

Dartmouth College Dartmouth Digital Commons

Open Dartmouth: Faculty Open Access Articles

10-20-2004

Location of the Optical Reverse Shock in the Cassiopeia A Supernova Remnant

Jon A. Morse
Arizona State University

Robert A. Fesen
Dartmouth College

Roger A. Chevalier
University of Virginia

Kazimierz J. Borkowski
North Carolina State University

Follow this and additional works at: <https://digitalcommons.dartmouth.edu/facoa>

 Part of the [Stars, Interstellar Medium and the Galaxy Commons](#)

Recommended Citation

Morse, Jon A.; Fesen, Robert A.; Chevalier, Roger A.; and Borkowski, Kazimierz J., "Location of the Optical Reverse Shock in the Cassiopeia A Supernova Remnant" (2004). *Open Dartmouth: Faculty Open Access Articles*. 2255.
<https://digitalcommons.dartmouth.edu/facoa/2255>

This Article is brought to you for free and open access by Dartmouth Digital Commons. It has been accepted for inclusion in Open Dartmouth: Faculty Open Access Articles by an authorized administrator of Dartmouth Digital Commons. For more information, please contact dartmouthdigitalcommons@groups.dartmouth.edu.

LOCATION OF THE OPTICAL REVERSE SHOCK IN THE CASSIOPEIA A SUPERNOVA REMNANT¹

JON A. MORSE,^{2,3} ROBERT A. FESEN,⁴ ROGER A. CHEVALIER,⁵ KAZIMIERZ J. BORKOWSKI,⁶
CHRISTOPHER L. GERARDY,⁷ STEPHEN S. LAWRENCE,⁸ AND SIDNEY VAN DEN BERGH⁹

Received 2004 May 14; accepted 2004 June 23

ABSTRACT

We use two epochs of *Hubble Space Telescope* WFPC2 images separated by 2 yr to determine the location and propagation of the reverse shock (RS) in the young supernova remnant Cassiopeia A (Cas A). The images trace optical line emission from fast-moving knots and filaments of highly processed ejecta as they cross the RS, become heated and compressed, and radiatively cool. At numerous positions around the optical shell, new emission features are seen in the 2002 images that were not yet visible in the 2000 exposures. In a few instances emission features seen in the first epoch have completely disappeared in the second epoch. We concentrate on two regions along the rim of the main emission shell in Cas A for close inspection: one in the northwestern part of the shell and another along the southwestern part of it. In these regions the RS is viewed almost edge-on, and its precise position has been measured. The RS is coherent in these regions over arcminute (~ 1 pc) scales but is highly distorted perpendicular to the direction of expansion. We find the RS to be generally expanding at 50%–60% of the ~ 5500 km s⁻¹ bulk velocity of the optical ejecta. We present shock models for the ejecta that are consistent with the high densities and short cooling times observed in the optical knots of the Cas A remnant.

Subject headings: ISM: individual (Cassiopeia A) — ISM: kinematics and dynamics — supernova remnants

1. INTRODUCTION

Cassiopeia A (Cas A) is the remnant of a core-collapse supernova (SN) of Type Ib/c or Type II that occurred in the late 17th century. An X-ray point source that is believed to be a neutron star associated with its progenitor (Tananbaum 1999; Murray et al. 2002) is located near the center of the main shell of optical, X-ray, and radio emission. In addition to fast-moving knots (FMKs) that exhibit extreme O, Si, S, Ar, and Ca (Chevalier & Kirshner 1978, 1979; Arendt et al. 1999), Fe-rich ejecta have also been identified in *Chandra* X-ray images (Hughes et al. 2000), which suggests that there was convective overturn of a significant portion of the progenitor core during the SN explosion. Slower moving He- and N-rich clumps (quasi-stationary flocculi, or QSFs) of circumstellar material (Chevalier & Kirshner 1978, 1979) and high-velocity, N-rich outer knots (Fesen et al. 1987; Fesen 2001) indicate that the progenitor may have been a WN-type Wolf-Rayet star that underwent significant mass loss during the late stages of stellar

evolution (Langer & El Eid 1986; Schaeffer et al. 1987; Fesen & Becker 1991; García-Segura et al. 1996; Vink et al. 1996). At a distance of ~ 3.4 kpc (Reed et al. 1995; Lawrence et al. 1995), Cas A is one of the most important laboratories for studying both the early stages of supernova remnant (SNR) evolution and the byproducts of explosive nucleosynthesis that enrich the interstellar medium (ISM).

The optical and X-ray line emission from the bright main emission shell are produced by SN ejecta that are excited by the reverse shock (RS). X-ray, radio, and infrared continuum emissions in the main shell are generated by synchrotron-emitting electrons that are trapped and accelerated in magnetic fields compressed by the shocks. High-resolution radio observations of synchrotron emission with the Very Large Array (VLA) (Anderson & Rudnick 1995) and of X-rays with *Chandra* (Gotthelf et al. 2001) have isolated emission from the sharp outer boundary of the forward blast wave as it encounters the circumstellar medium (CSM). However, isolating a similar inner boundary pinpointing the precise location of the RS has proved to be elusive, primarily because of complicated line-of-sight projection effects.

In this paper, we present optical emission-line images of Cas A obtained with the Wide Field Planetary Camera 2 (WFPC2) aboard the *Hubble Space Telescope* (*HST*) at two epochs that show stellar ejecta becoming radiative after crossing the RS. In several locations around the remnant, the RS projects edge-on to a sharp but highly distorted structure. New emission is observed in our second epoch images as stellar ejecta cross the RS and begin to radiate in the postshock zone. We present the *HST* data sets in § 2, analyze two locations in the remnant where the RS can be seen in an edge-on viewing geometry in § 3, and discuss physical parameters of the RS and models for the radiative ejecta in § 4. Finally, we summarize our conclusions in § 5.

2. OBSERVATIONS

We imaged the Cas A SNR using the *HST* WFPC2 during nine orbits on 2000 January 23 (epoch J2000.06) and again on

¹ Based on observations with the NASA/ESA *Hubble Space Telescope* obtained at the Space Telescope Science Institute, which is operated by the Association of Universities for Research in Astronomy, Inc., under NASA contract NAS5-26555.

² Center for Astrophysics and Space Astronomy, University of Colorado, 389 UCB, Boulder, CO 80309.

³ Current address: Department of Physics and Astronomy, Arizona State University, Box 871504, Tempe, AZ 85287-1504; jon.morse@asu.edu.

⁴ Department of Physics and Astronomy, Dartmouth College, Hanover, NH 03755.

⁵ Department of Astronomy, University of Virginia, P.O. Box 3818, Charlottesville, VA 22903.

⁶ Department of Physics, North Carolina State University, Raleigh, NC 27695.

⁷ McDonald Observatory, 1 University Station, C1402, Austin, TX 78712-0259.

⁸ Department of Physics and Astronomy, Hofstra University, Hempstead, NY 11549.

⁹ Dominion Astrophysical Observatory, Herzberg Institute of Astrophysics, National Research Council of Canada, 5071 West Saanich Road, Victoria, BC V9E 2E7, Canada.

TABLE 1
WFPC2 FILTERS, DETECTED EJECTA LINE EMISSIONS, AND EXPOSURE TIMES

Filter	Bandpass (Cut-on–Cutoff) (Å)	Primary Lines	Secondary Lines	Exposure Times (2000, 2002 Epochs) (s)
F450W.....	3700–5200	[O III] $\lambda\lambda$ 4959, 5007	[O II] $\lambda\lambda$ 3726, 3729	4 × 700
F675W.....	6000–7600	[S II] $\lambda\lambda$ 6716, 6731 [O II] $\lambda\lambda$ 7319, 7330	[N II] $\lambda\lambda$ 6548, 6583; H α λ 6563 [Ar III] λ 7135; [O I] $\lambda\lambda$ 6300, 6364	4 × 500
F850LP.....	8300–10600	[S III] $\lambda\lambda$ 9069, 9531	[S II] $\lambda\lambda$ 10287–10370	4 × 700

2002 January 16 (epoch J2002.04). The 2000 images were discussed in detail in Fesen et al. (2001). We employed broad rather than narrow passband WFPC2 filters, including F450W, F675W, and F850LP, in order to capture the full velocity range of the emitting ejecta. The primary emission lines traced by these filters in the FMKs were [O III] $\lambda\lambda$ 4959, 5007, [S II] $\lambda\lambda$ 6716, 6731, and [S III] $\lambda\lambda$ 9069, 9531, respectively. Other emission lines were present in the bandpasses at typically much lower relative flux levels; the main exceptions were strong [O II] $\lambda\lambda$ 7319, 7330 emission from oxygen-rich FMKs and [N II] $\lambda\lambda$ 6548, 6583 emission from nitrogen-rich QSFs, both falling within the F675W bandpass. Fesen et al. (2001) discuss the emission lines contained in each filter in detail. Table 1 summarizes these observations, listing the three filters used in this study along with their full width at zero-intensity (FWZI) bandpasses, exposure times, and principal ejecta line emissions within the bandpass.

The optical remnant of Cas A subtends $\sim 4'$ diameter on the sky, so that several offset pointings with WFPC2 were required to cover the bright emitting regions. For the 2000 image set, all three filters (plus a fourth, F658N) were used at three WFPC2 positions, covering the northeast, northwest, and southwest rims of the main shell. Remnant shell regions adjacent to each of the three main target positions were also imaged in the F675W filter. For the 2002 image set, we excluded the F658N filter, since we could not identify the slow-moving nitrogen-rich QSFs based on the first-epoch F658N images and the small proper motions seen between the two epochs of F675W images. We obtained exposures in all three broad filters at four offset pointings that covered most of the main optical shell and the base of the northeast jet. For both data sets, the images from all offset pointings were reduced separately, flux calibrated, corrected for geometric distortions, and mosaicked together into single, large images using the procedures described in Fesen et al. (2001). Figure 1 shows the 2002 F675W mosaic of the main ejecta shell. We focus on two regions, along the northwest and southwest rims, for detailed study.

3. REVERSE SHOCK LOCATION

There were numerous changes between 2000 and 2002 throughout the bright ejecta shell seen in Figure 1. Most changes were subtle intensity variations, usually decreases, in filaments that we can track in both epochs, which we interpret as radiative recombination and cooling of post-RS gas. However, some changes were quite dramatic, with new filaments appearing in the 2002 images where no emission existed in the 2000 images. We interpret this phenomenon as ejecta that have crossed the RS at some time between 2000 January and 2002 January (ignoring the light travel time of 11,000 yr to Earth), became heated, ionized, and subsequently radiatively cooled and compressed. Relatively short cooling times result from the

high densities and metal-rich composition of the ejecta. (We discuss the shock physics in more detail in § 4.) At a few locations around the main shell, where the ejecta expand nearly transverse to our line of sight, our viewing angle allows us to see this process occur in an edge-on geometry. Such regions correspond, as expected, to locations along the shell that show radial velocities near the remnant mean velocity in the Fabry-Pérot data cube of Lawrence et al. (1995). We discuss the two regions shown in detail in the bottom panels of Figure 1 in the following subsections.

3.1. The Northwest Rim

The northwest rim region shown in Figure 2 was noted by Fesen et al. (2001) as likely marking the location of the RS. Their speculation was based primarily on morphology: The inner edge toward the SNR center is sharp and composed largely of wavy filaments aligned transverse to the flow direction. Further along the flow in the expansion direction, the network of filaments transitions to a series of Rayleigh-Taylor-like radially aligned features. This ensemble appears to show a time sequence, with gas distributed at the various stages of postshock heating and compression becoming dynamically unstable and fragmenting into radial clumps as the gas radiatively cools. Fesen et al. (2001) predicted that if the inner edge of this northwest filament indeed marks the location of the RS, its proper motion outward from the SNR center in a second-epoch image should be somewhat less than that of the bulk motion of individual filaments. This is precisely what is observed.

In the top left panel of Figure 2 we mark four regions along the inner edge of the northwest filament where new radiating features have emerged in the 2002 epoch image. These four regions are magnified for close scrutiny in the bottom panels.¹⁰ The first two panels in each left-to-right series display the original images with identical logarithmic intensity stretches. The third image shows the intensity differences after the bulk motions have been removed; that is, the radiative filaments in the 2000 image were shifted to align with the corresponding structures in the 2002 image, and the images were subtracted. White in the difference images indicates brighter emission in 2000, and black indicates new emission in 2002.

All along the northwest filament, when the bulk motions were removed and the images subtracted, the previously known radiating features generally canceled or were somewhat brighter in the 2000 image, usually by only 1%–10%. The new

¹⁰ It was necessary to divide this filament, and later the southwest filament, into subregions for closer analysis because of the differential velocities along the structure. Fesen et al. (2001) noted the north-to-south radial-velocity gradient from +900 to +600 km s⁻¹ of this feature in the Fabry-Pérot data cube of Lawrence et al. (1995). Each of the subregions highlighted in Fig. 2 also has a slightly different bulk proper motion vector away from the expansion center, such that it was not possible to align the 2000 image of the entire northwest filament with the 2002 image by using a single (X, Y) translation.

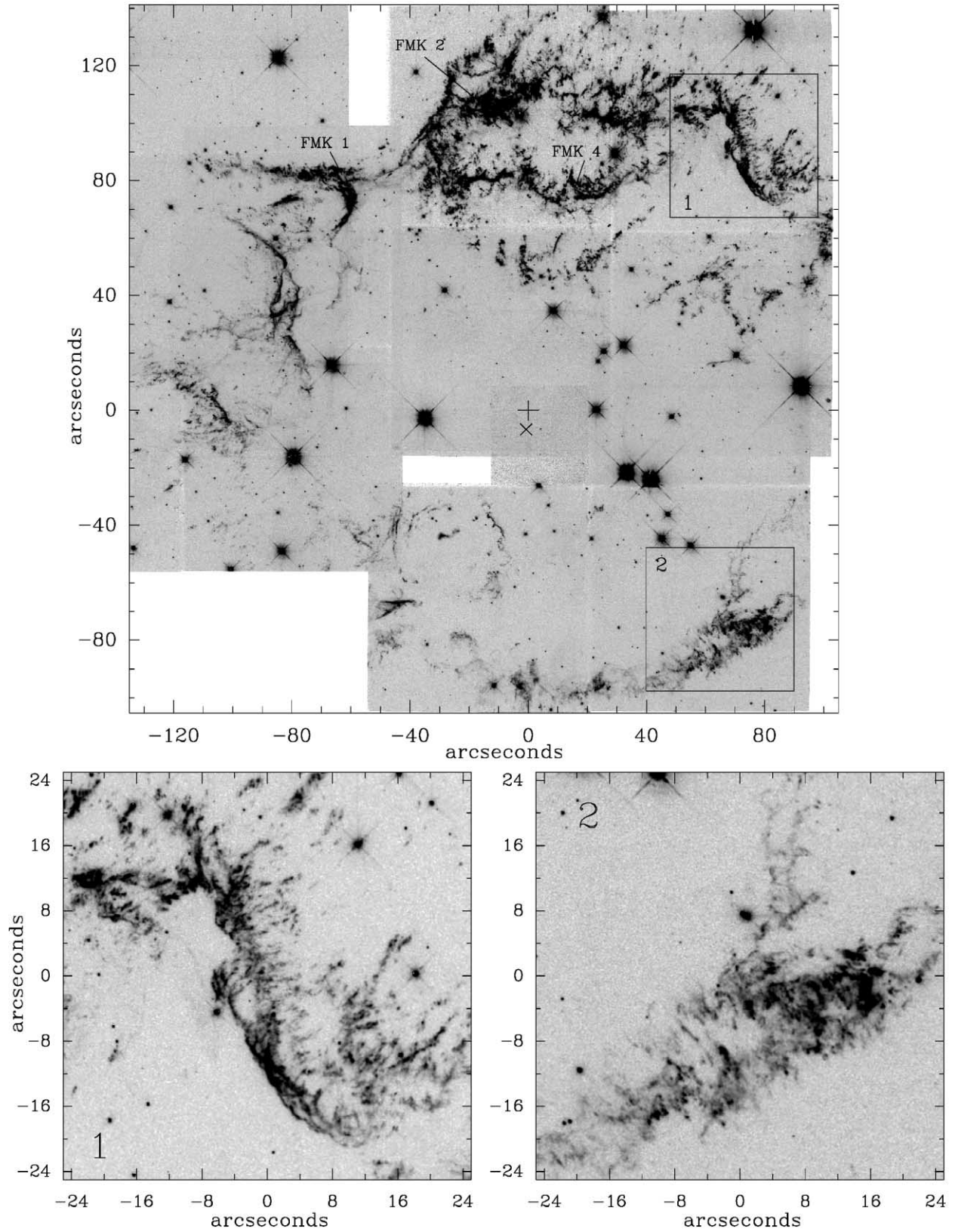


FIG. 1.—WFPC2 F675W mosaic of Cas A showing the main optical shell of ejecta. North is to the top, east is to the left, and logarithmic intensity stretches are used. Areas where the RS propagates nearly transverse to the line of sight are highlighted in the boxes. A plus sign at (0, 0) in the top plot marks the SNR expansion center of Thorstensen et al. (2001) at coordinates $\alpha(\text{J2000}) = 23^{\text{h}}23^{\text{m}}27^{\text{s}}.77$, $\delta(\text{J2000}) = 59^{\circ}48'49''.4$. The cross (\times) marks the position of the X-ray point source $\sim 6''.5$ south of the expansion center along P.A. 174° .

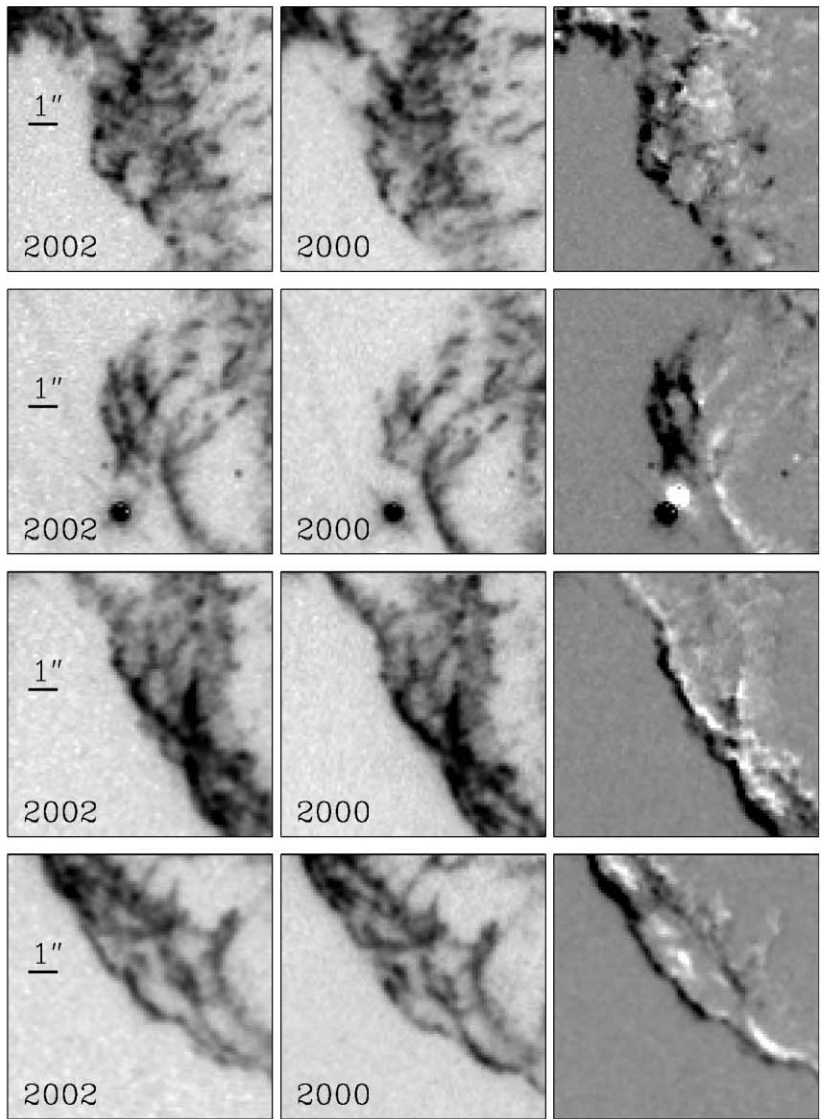
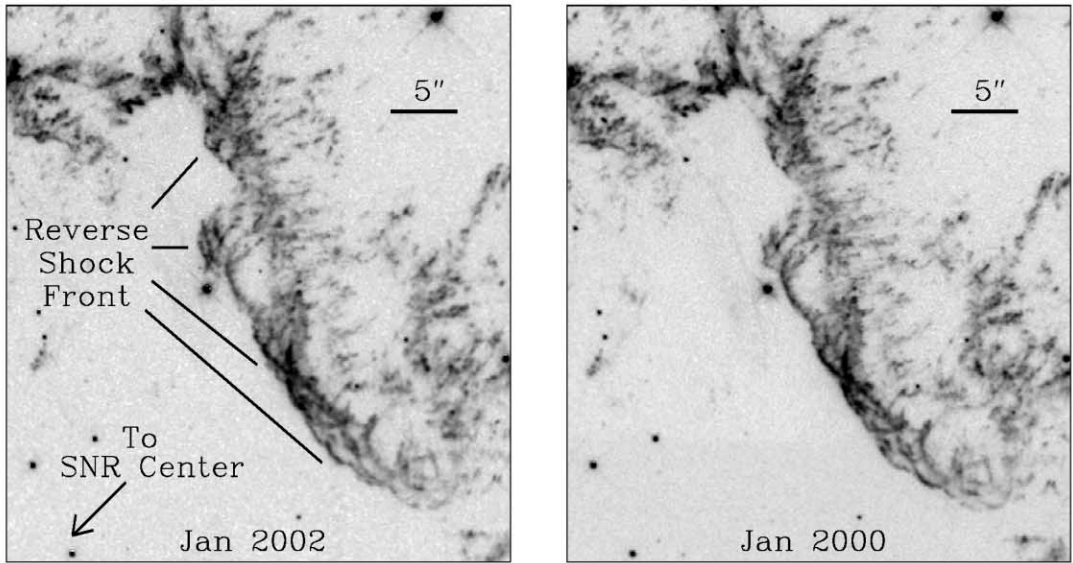


FIG. 2.—*Top panels*: Both epochs of WFPC2 F675W images of the northwest rim region; the favorable viewing geometry shows a very sharp inner edge to the line emission where material has recently crossed the RS. The epochs were aligned using stars as tie points, and the $\sim 0''.5\text{--}0''.7$ proper motions of the fast ejecta away from the SNR center can be discerned relative to the stationary stars. Four small subregions along the RS front are highlighted in the bottom panels. See the text for details.

emission features in the 2002 image, shown in black in the difference images, generally appeared along the inner edge of the filament. We interpret the new features as recently shocked stellar ejecta that now radiate in the post-RS region. Assuming that our viewing angle is roughly edge-on, we can estimate the speed of the RS relative to the bulk motion by measuring the width of the region containing the new emission features:

$$V_{\text{RS}} = V_{\text{trans}} - \Delta r / \Delta t, \quad (1)$$

where V_{RS} is the RS velocity, V_{trans} is the transverse velocity derived from the bulk proper motion (assuming that the shock velocity in the optically emitting clumps is comparatively small and does not appreciably alter the bulk expansion velocity; see § 4), Δr is the width in kilometers of the new emitting region, and Δt is the time interval in seconds between observations. The quantities on the right side of the equation can be measured from the *HST* observations.

The bulk proper motions of the emitting features in the northwest filament are $\sim 0''.31\text{--}0''.34 \text{ yr}^{-1}$, corresponding to transverse velocities of $\sim 5000\text{--}5500 \text{ km s}^{-1}$ at a distance of 3.4 kpc. Each of the four subregions in the lower panels of Figure 2 subtends $9'' \times 9''$. The expansion vector for each subregion differs in direction, as expected, due to the extent of the filament; all motions are directed away from the SNR expansion center marked in Figure 1 (see Thorstensen et al. 2001). An example of the magnitude and direction of the image shifts over the 2 yr observing period is given by the $\sim 0''.65$ offsets of the stationary stars (one bright and one faint) in the difference image of the second series.

Estimating the width Δr of the region of new emission is complicated by photometric variations in the existing features and imprecise knowledge of our true viewing geometry along the filament. Examples of the former effect can be seen in the fourth (bottom) subregion series in Figure 2. The southernmost arc is much brighter in the 2000 image and appears white in the difference image. This area harbors two fainter arcs in the 2002 image. Probably the original arc became fainter as the shocked material cooled and the shock propagated across the arc (see the discussion in § 4). A second arc has formed where new material has crossed the RS. However, with only two epochs, we cannot distinguish this scenario from one in which the original arc in 2000 was bright because of a chance projection of two arcs. Differential motions could then have resulted in the feature appearing as two distinct but fainter features in the 2002 image. Meanwhile, immediately above, in the middle arc of this subregion, the emission in the 2002 image was brighter than in the 2000 image, and hence appears black in the difference image. However, this photometric change does not appear to result from the appearance of a new ejecta feature.

We estimate the width Δr by concentrating on areas where new ejecta filaments appear in 2002 where none existed previously. By definition, such features appear black in the difference images (excluding those black features that had fainter counterparts in 2000). New emission features appear in all four of the subregions magnified in the lower panels of Figure 2. The inner edge of emission in the first (top) series is very sharp in both epochs. Several new emission knots and arcs appear in the 2002 image. In the second series, new filaments appear in 2002 as extensions of several stubby features in the 2000 image like new branches on a tree. Although a dramatic example of new emission in 2002, we suspect that our viewing geometry at this specific area may depart from edge-on. In the third

series, the brightest filament becomes thicker toward the inner edge, and two small arcs or protrusions appear. In the fourth series, the filament immediately to the right of the $1''$ label is new. The best areas for measuring the width are, therefore, based on these new features in the first, third, and fourth series.

The width Δr is essentially the amount by which the RS has propagated inward in the reference frame of the expanding ejecta. If Δr is smaller than the bulk proper motion distance traveled by the ejecta, then the RS expands outward from the SNR center at a rate that is less than the ejecta expansion velocity. If $\Delta r = 0$, then the RS travels outward at the same velocity as the ejecta; i.e., there would be no shock. If Δr is equal to the bulk proper motion distance, then the RS would appear to be stationary in our observing reference frame. Finally, if Δr is larger than the bulk proper motion distance, we would see the RS moving inward toward the SNR center. Throughout the northwest filament region, and in the southwest rim region described below, the difference images show that Δr usually appears to be somewhat less than half of the bulk proper motion distance. This can also be seen by blinking the aligned images. At a few places, however, particularly with the bubble-like feature in the middle of the first subregion of Figure 2, Δr is as large as the bulk proper motion distance (≥ 6 pixels); that is, new emission appears at the same pixel position in the 2002 image as previous features did in the 2000 image. If our viewing geometry is edge-on, we conclude that the RS, although largely contiguous, propagates differentially at subarcsecond scales. Such motions would naturally lead to its highly contorted appearance over larger scales.

The typical width Δr of the new emission region in the difference images of Figure 2 is about the width of a radiative arc, $\sim 2\text{--}3$ pixels or $\sim 30\%\text{--}45\%$ of the bulk proper motion distance. Another illustration is presented in Figure 3, where we have rotated clockwise a portion of the northwest filament contained in the bottom two subregions of Figure 2 so that the expansion direction is left to right. The emission intensities have been scaled to high contrast so that individual arcs and knots are saturated and the sharp edge of the filament is highlighted. The rightmost panel magnifies a section of the filament so that individual pixels can be discerned. The top of this panel is from the 2000 image and the bottom of the panel is from the 2002 image. The existing features moved $\sim 6\text{--}7$ pixels to the right over the 2 yr baseline, but the edge of the filament moved only ~ 3.5 pixels to the right because new emission appeared. We mark this difference between the bulk proper motion distance and Δr , denoted here by $(|\mu| - |\Delta r|)$; thus $\Delta r \approx 3$ pixels = $0''.3$.

Based on these estimates, we then derive a Δr of $\sim 1\text{--}1.5 \times 10^{11} \text{ km}$, and the time between observations $\Delta t \approx 6.25 \times 10^7 \text{ s}$. Using equation (1) and assuming that the timescale for the postshock ejecta to become radiative is shorter than the period between observations, the values for V_{trans} , Δr , and Δt imply a typical RS expansion velocity of $V_{\text{RS}} \approx 5000\text{--}2000 = 3000 \text{ km s}^{-1}$ at the location of the northwest filament.

3.2. The Southwest Rim

We observe RS emission features in the southwest rim region similar to those in the northwest filament. New emission appears in the 2002 image where none had previously been seen, and the interface over which the new features have crossed appears sharp and coherent over scales much larger than individual knots. Figure 4 shows the southwest rim region in detail, with two subregions magnified in the lower panels.

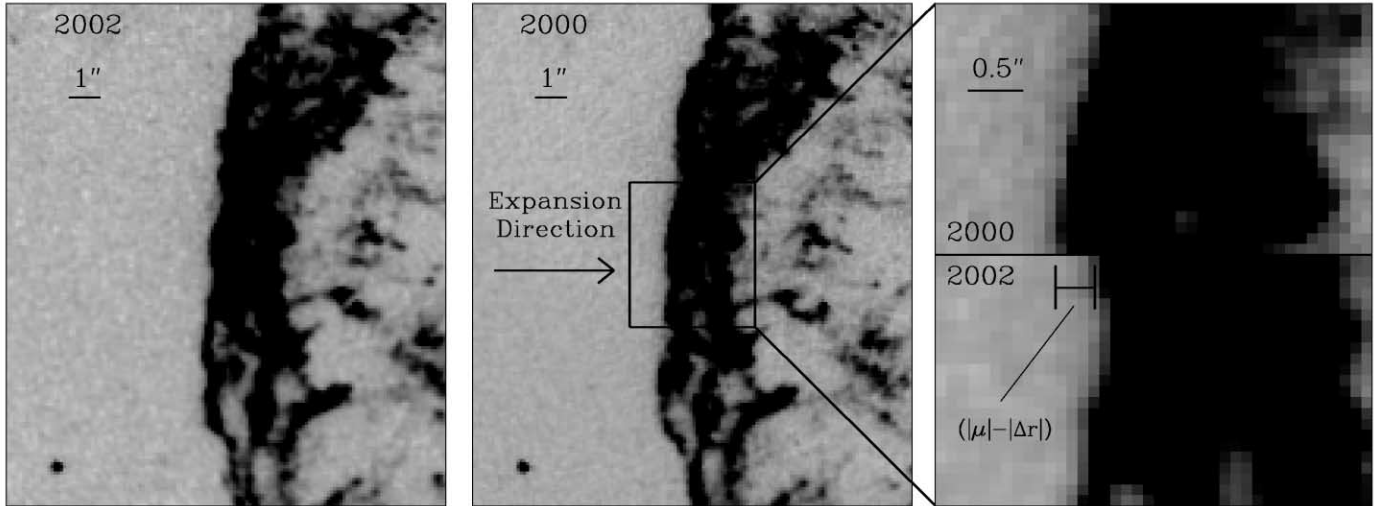


FIG. 3.—WFPC2 F675W images of the northwest filament rotated clockwise $\sim 38^\circ$ so that the expansion direction is approximately left to right. The left and middle panels subtend an area encompassing the bottom two subregions in Fig. 2, with the inverse intensity levels set to very high contrast so that the edges of the emission are clearer. The right panel magnifies the center of the filament and displays the 2000 epoch image in the top of the frame and the 2002 epoch image in the bottom of the frame. The proper motion distance the emission features have traveled between the two epochs is 6–7 pixels. We mark the difference between the proper motion distance and the distance that the RS has traveled backward in the ejecta frame of reference, expressed as $(|\mu| - |\Delta r|)$.

The bulk motion of the emitting debris can be discerned relative to the stationary stars and to a low-velocity QSF knot. In order to align the existing emission features in the two subregions in the lower panels of Figure 4, we translated the 2000 images by proper motions over the 2 yr baseline of ~ 5.1 – 5.4 pixels directed away from the SNR expansion center, corresponding to transverse velocities for this fast-moving material of $V_{\text{trans}} \approx 4200$ – 4400 km s^{-1} . The smaller transverse velocities in these regions, compared to those in the northwest filament, may indicate that we are not viewing the emission precisely edge-on. The subregions in Figure 4 show radial velocities of ~ 500 – 1000 km s^{-1} blueshifted from the remnant mean in the Fabry-Pérot data cube of Lawrence et al. (1995), and we therefore view this material not exactly face-on (inclination $\sim 75^\circ$ – 80°).

The first subregion in Figure 4 displays a vertically oriented complex of faint emission features. Each panel in this series is $9'' \times 15''$. Inspection of the two original images and the difference image shows that a thin ribbon of new emission ~ 2 pixels across is present in the 2002 image. In the bottom subregion of Figure 4, the RS projects roughly across the diagonal of the $14'' \times 14''$ images. There are several examples of new emission knots in the 2002 image that appear black in the difference image.

Our estimates of the width Δr of the new emission are hampered by the partially face-on orientation of the inner edge of the southwest rim region. Nevertheless, similar to the northwest filament, we observe the RS propagating outward with a speed $\sim 60\%$ – 70% of the bulk motion of the optically emitting ejecta features. Other regions around the bright main shell of Cas A show similar emission features emerging from a thin RS, usually with even less favorable viewing geometries. In the following discussion we analyze the implications of our observations for understanding the excitation mechanism, morphology, and dynamics of the Cas A SNR.

4. DISCUSSION AND METAL-RICH SHOCK MODELS

Cas A is a young SNR in the ejecta-dominated phase of its evolution. A forward blast wave is driven ahead of the

expanding ejecta into the CSM, and it has begun to slow to velocities below the free expansion velocities of the fast ejecta as CSM material is swept up. The cold ejecta expand supersonically outward from the explosion center, and an RS has formed well behind the forward shock that decelerates the impinging ejecta. In totality, Cas A is a textbook case of forward/reverse shock structure, although details of the interaction physics and evolution are complex (e.g., Chevalier 1982; Borkowski et al. 1996; Blondin et al. 2001).

The *Chandra* X-ray images (Gotthelf et al. 2001) and high-resolution VLA radio synchrotron maps (Anderson & Rudnick 1995) of Cas A show a thin outer edge to the SNR that has been interpreted to represent the forward shock where the blast wave encounters the CSM (DeLaney & Rudnick 2003). The main emission shell seen in X-rays and radio arises from post-RS ionization and compression of ejecta gas and from electron acceleration in the compressed magnetic fields. The forward shock is a reasonably smooth and coherent structure around the perimeter of the SNR as compared to the extreme clumpiness of the post-RS shell (PRSS) of ejecta. At a few locations we can measure the distance between the RS and the forward shock. The northwest filament lies at a projected distance of $\sim 1.8 \text{ pc}$ (slightly less than $2'$; Fig. 1) from the SNR expansion center, and the projected distance from the inner edge of the northwest filament to the outer boundary of the X-ray/radio edge demarcating the forward blast wave is $\sim 0.9 \text{ pc}$ (slightly less than $1'$; DeLaney et al. 2004). Somewhere between the RS and the forward blast wave lies a contact discontinuity in which the pressure balances between the shocked CSM and the shocked ejecta. In reality the contact discontinuity is probably very distorted and difficult to identify as a coherent structure (e.g., Blondin 2001).

The precise location of the RS is difficult to discern at X-ray and radio wavelengths because of the thickness of the emitting shell combined with the three-dimensional nature of the SNR. In addition, Blondin et al. (2001) show in their three-dimensional hydrodynamical simulations of young SNR evolution that when FeNi bubbles are included in the composition of the ejecta, the RS is severely deformed. At visible

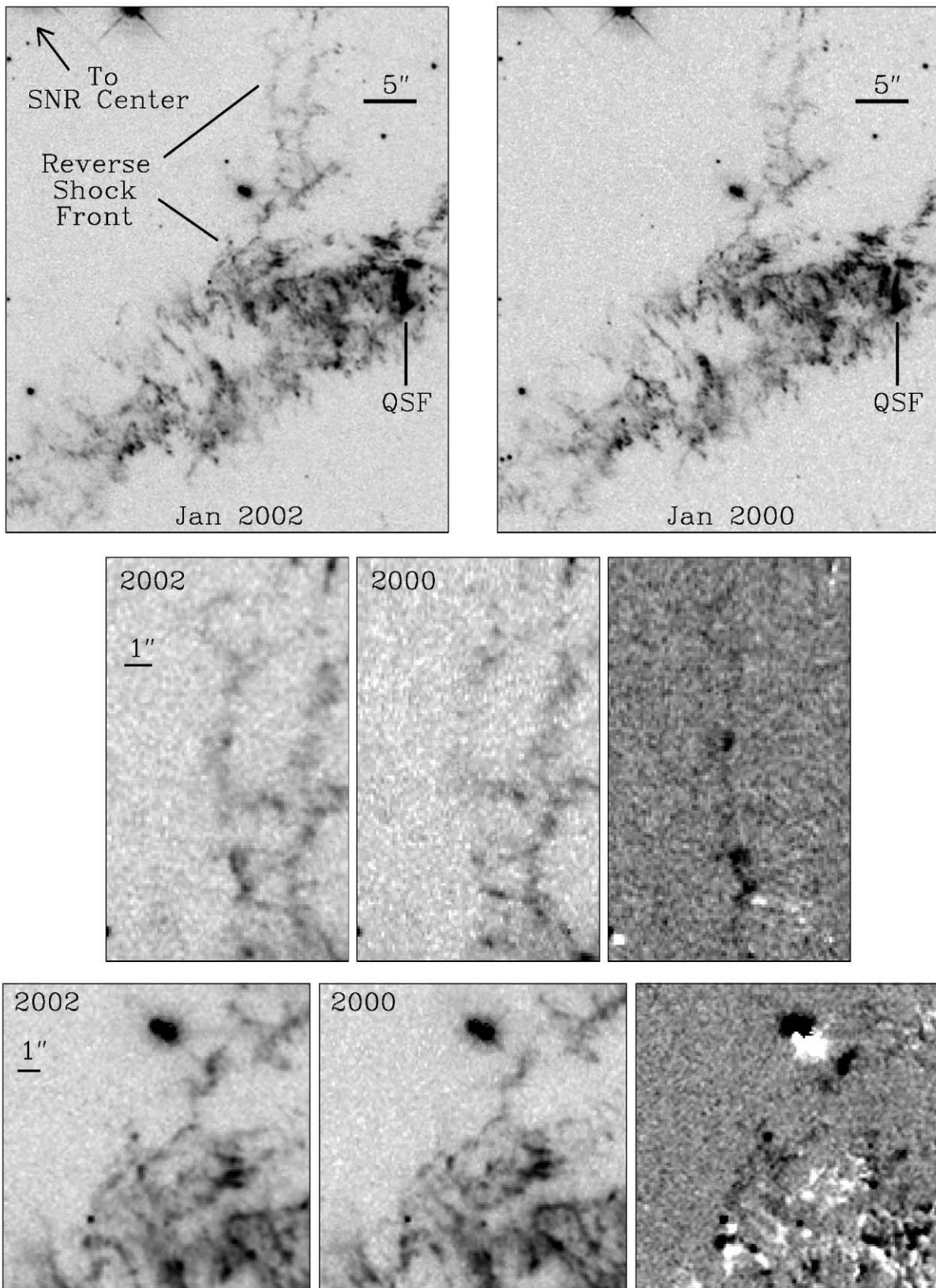


FIG. 4.—*Top panels*: Both epochs of WFPC2 F675W images of the southwest rim region. The viewing geometry is also favorable for observing new emission just behind the RS, but here the new emission is much fainter than in the northwest filament. As in Fig. 2, the epochs were aligned using stars as tie points, and the proper motions of the fast ejecta away from the SNR center can be discerned relative to the stationary stars. A slow-moving QSF filament is noted. Two subregions along the RS front are highlighted in the bottom panels. See the text for details.

wavelengths, the emitting features trace the densest post-RS ejecta (see below). In the [S II] Fabry-Pérot data cube of Lawrence et al. (1995), the optical emission is largely confined to ringlike structures on the surface of an expanding shell, which may signify the presence of large bubble-like structures in the ejecta. Because the covering fraction of the optically emitting shell is low, we can focus on regions where the viewing geometry is favorable in order to isolate the RS at specific locations. The northwest and southwest rim regions discussed in §§ 3.1 and 3.2 are prime examples.

Cold, freely expanding ejecta encounter a density and velocity discontinuity at the RS and are decelerated. The shock velocity, V_s , experienced by a parcel of ejecta depends on the gas number density, n_{ej} , in the parcel according to $n_{\text{ej}}V_s^2 = \text{const.}$, assuming that the ram pressure at the RS is constant over scales larger than an individual knot or clump ($\sim 10^{16}$ cm; see Figs. 2 and 4 and Fesen 2001). In fact, although highly contorted (at least in projection), the RS at the location of the northwest filament in Figure 2 appears sharp, smooth, and coherent over arcminute ($>10^{18}$ cm ≈ 1 pc) linear scales. The optical emission we observe in the PRSS traces the evolution of denser clumps with relatively low shock velocities and short cooling times, but we also assume that these ejecta fragments represent the high-density range of a continuous ensemble of ejecta gas densities. The very clumpy appearance of the X-ray-emitting ejecta in the *Chandra* images (Hughes et al. 2000) suggests that substantial density variations persist to low gas densities. Since the ejecta were launched essentially instantaneously by the SN explosion $\gtrsim 300$ yr ago, all the material crossing the RS in a particular location at this time has the same expansion velocity, independent of the gas density.

We can estimate postshock densities and ionization conditions in the optically emitting ejecta from spectrophotometry (Peimbert & van den Bergh 1971). Hurford & Fesen (1996) measured emission-line ratios and extinction toward several FMKs in the northern ring of optical ejecta in Cas A. Using shock models, we can then match the observed spectra to derive preshock densities, shock velocities, relative abundances, compressions, and cooling times and distances (cf. Vancura et al. 1992; Hartigan et al. 1994). The emitting metal-rich ejecta (i.e., devoid of H and He) in O-rich SNRs have been modeled as shock waves (Itoh 1981, 1986; Dopita et al. 1984; Borkowski & Shull 1990; Blair et al. 2000), cool gas photoionized by the SNR X-rays (Blair et al. 1989, 1994), or the combination of a shock wave and its photoionized precursor (Sutherland & Dopita 1995). Here we use the method of Blair et al. (2000) to model the emission as an ensemble of radiative planar shock waves, employing a modified version of the J. Raymond shock code. (We refer the reader to § 3.2 of Blair et al. [2000] for a detailed discussion of the metal-rich shock models and spectral matching technique.)

The radiative cooling rate is much higher in metal-rich plasmas than in ordinary (H-bearing) astrophysical plasmas, at least at postshock temperatures low enough so that key coolants such as O, Ne, S, etc. remain in ionization states below He-like (e.g., Sutherland & Dopita 1995). The electron temperature remains fairly constant through much of the postshock emitting zone, and the ionization state established there does not have time to respond when the temperature finally drops because the recombination times are much longer than the radiative cooling times. A single shock velocity thus tends to produce bright emission from one or two ionization states. Because we observe emission from a wide range of ionization states, we infer a wide range of shock velocities and

hence ejecta gas densities. Low gas densities result in high shock velocities that produce high postshock temperatures and ionization to H-like and He-like states with relatively long cooling times. High gas densities result in lower shock velocities and lower ionization states with short radiative cooling times. Thus, we predict that at the spatial resolution of $0''.1$ – $0''.2$ ($\sim 10^{16}$ cm) in our *HST* images, the optical ejecta knots and arcs should not be strongly correlated with X-ray-emitting ejecta, but rather should be adjacent near the RS. However, because the deceleration experienced by the gas is proportional to the shock velocity, the denser, optically emitting knots should pull away from the low-density neighboring gas over time. It is possible that we could observe this differential motion using future high-resolution optical and X-ray observations.

Table 2 lists dereddened emission-line ratios observed for the optical FMK 1, FMK 2, and FMK 4 knots (identified in Fig. 1) from Hurford & Fesen (1996) and from three grids of planar shock models. Each grid of models was calculated keeping the ram pressure $n_{\text{ej}}V_s^2 = \text{const.}$ at values of 1×10^5 , 5×10^5 , and 1×10^6 km s $^{-1}$ cm $^{-3}$, respectively, over a range of shock velocities from 20 to 1000 km s $^{-1}$, although shocks above ~ 200 km s $^{-1}$ contributed little or no optical emission.¹¹ The preshock number densities (i.e., the total number of nucleons per unit volume crossing the shock, with oxygen as the primary constituent) were anchored at $n_{\text{ej}} = 10$, 50, or 100 cm $^{-3}$ for a shock velocity of 100 km s $^{-1}$ in each grid. A constant magnetic parameter $B/(n_{\text{ej}}^{1/2}) = 1.0$ $\mu\text{G cm}^{3/2}$ (moderate B field; see Sutherland et al. 1993; Sutherland & Dopita 1995) was assumed for each model, and the cooling times were not allowed to exceed 35 yr (the observed fading timescale for the optical knots; van den Bergh & Kamper 1985). The magnetic parameter affects the postshock compression, hence the cooling times; in fact, our choice of B field yields short cooling times of days to months for the fully radiative shocks. Synchrotron emission is observed in the PRSS, so magnetic fields must be present. However, the adiabatic expansion of the ejecta from the time of the explosion argues that the B fields in the ejecta at the time they cross the RS could be vanishingly small, and a pure hydrodynamic description of the shock physics could be adequate. Nevertheless, using these shock parameters and the iterative methods described in Blair et al. (2000), we achieved a reasonable match of the GRID-1E6 line ratios to the FMK 1 observations using the abundance set and power-law weighting scheme for combining the flux ratios from the individual planar models listed in footnote b to Table 2.

Although the model parameters derived to match the FMK 1 observations are likely to be different than would be found for the northwest filament or elsewhere (especially the abundances), we present the FMK 1 modeling results as an example of the range of gas densities and shock velocities that we expect to be common to all of the optically emitting ejecta in Cas A. Despite being compressed and subject to a variety of

¹¹ Recall from the Rankine-Hugoniot relations that for a strong shock, the postshock temperature $T = (3/16)(\mu m_{\text{H}}/k_{\text{B}})V_s^2$, where μ is the mean molecular weight, m_{H} is the mass of hydrogen, k_{B} is Boltzmann's constant, and V_s is the shock velocity. While μ generally falls between 0.5 and 1.4 for normal (cosmic) abundance ISM gas, for highly metal-rich plasmas μ could range between ~ 2 and 20, depending on the composition of the gas and the ionization state as it enters the shock. Hence, the postshock temperature is generally much higher for a given shock velocity, and even moderate-velocity metal-rich shocks ($\gtrsim 200$ km s $^{-1}$) achieve high ionization states and produce mainly X-ray emission.

TABLE 2
OBSERVED (DEREDDENED) AND MODEL LINE RATIOS FOR CAS A EJECTA KNOTS

Ion	λ	FMK 1 ^a	FMK 2 ^a	FMK 4 ^a	GRID-1E5 ^b	GRID-5E5 ^b	GRID-1E6 ^b
[O II].....	3727	420	234	161
[Ne III].....	3869	42	42	42
[S II].....	4068, 4076	41	51	35	27	36	39
[O III].....	4363	15	12	25	20	18	17
[O III].....	4959	100	100	100	100	100	100
[O III].....	5007	300	307	305	300	300	300
[O I].....	6300	20	19	27	2	2	2
[S II].....	6717, 6731	36	48	17	132	65	41
[Ar III].....	7136, 7750	11	18	9	15	14	13
[Ca II].....	7291	2	2	1	2	2	2
[O II] ^c	7325	62	57	169	42	52	56
[S III].....	9532	32	66	28	36	35	35
[S II].....	10400	27	33	23	18	24	26
[S II] ratio.....	6716/6731	0.80	0.57	0.52

^a Line ratios relative to [O III] $\lambda 4959 = 100$ from Table 2 in Hurford & Fesen (1996). See their paper for details of the observations, flux calibrations, and extinction corrections. Only the strongest features are presented. Variations in line ratios between the different FMKs could result from different gas densities, abundances, shock velocities, shock ages, magnetic field strengths, etc.

^b Planar shock model grids calculated with ram pressure $n_{\text{ej}} V_s^2 = \text{const.}$ values of 1×10^5 , 5×10^5 , and $1 \times 10^6 \text{ km s}^{-1} \text{ cm}^{-3}$, respectively, for all shocks in each grid. Each grid included shock velocities ranging from 20 to 1000 km s^{-1} , although shocks above $\sim 200 \text{ km s}^{-1}$ contributed little optical emission. The preshock number densities are anchored at $n_{\text{ej}} = 10, 50, \text{ or } 100 \text{ cm}^{-3}$ for a shock velocity of 100 km s^{-1} in each grid. A constant magnetic parameter $B/(n_{\text{ej}}^{1/2}) = 1.0 \mu\text{G cm}^{3/2}$ (moderate B field) and an initial electron-to-ion temperature ratio of $T_e/T_i = 0.4$ was assumed for each model. The line fluxes from the planar models in each grid were combined using a power-law weighting function $F \propto V_s^{-\alpha}$ with $\alpha = 0.35$, optimized here to provide a reasonable match between the FMK 1 and GRID-1E6 line ratios. The abundance set derived to achieve this match, on a logarithmic scale where H = [12.00], was O = [16.00], S = [14.90], Ar = [14.50], and Ca = [14.00]. Other abundances were set to He = [11.00], C = [14.80], Ne = [15.50], Mg = [14.80], Si = [14.70], Fe = [15.30], and Ni = [14.00] but are not constrained by the observations.

^c [O II] $\lambda\lambda 7320, 7330$ is blended with [Ca II] $\lambda 7324$ in the observations, although the contamination should be $< 10\%$ given the weakness of [Ca II] $\lambda 7291$.

hydrodynamic and radiative instabilities, the structure in the ejecta at both optical and X-ray wavelengths and the contorted shape of the RS suggest that the gas is highly inhomogeneous as it enters the shock, perhaps like a sponge with density peaks at the interstices between lower density regions.

For the optical ejecta, preshock number densities of $n_{\text{ej}} \sim 25\text{--}2500 \text{ cm}^{-3}$ and shock velocities in the range 20–200 km s^{-1} are needed to reproduce the optical emission-line spectra, including the [S II] $\lambda 6716/\lambda 6731$ ratios that are close to the high-density limit ($n_e \sim 10^4$; Peimbert & van den Bergh 1971). We note two consequences of these parameters: (1) The shock velocities experienced by the optically emitting ejecta are only a few percent of the free expansion velocities. Hence, the motions of the optically emitting ejecta fragments approximately represent the initial velocities imparted to the ejecta in the SN explosion. (2) The X-ray-emitting ejecta should generally have preshock number densities of $\sim 0.1\text{--}10 \text{ cm}^{-3}$ if the ram pressure at the RS is constant and the ejecta densities vary continuously.

In § 3.1 we estimated that the RS expansion velocity in the northwest filament was $\sim 3000 \text{ km s}^{-1}$, while the ejecta velocities were $\sim 5000 \text{ km s}^{-1}$. Hence, we infer that the typical gas density that experiences a shock velocity of $V_s \approx 2000 \text{ km s}^{-1}$ is $n_{\text{ej}} \approx 0.25 \text{ cm}^{-3}$. In other words, most of the mass and momentum are carried in the X-ray-emitting, low-density ejecta. The full range of electron densities observed in the PRSS is of the order of 10^5 (~ 0.1 to $> 10^4 \text{ cm}^{-3}$). Hydrodynamic simulations of radiative shocks (e.g., Sutherland et al. 2003) can generate a large range of densities in the postshock region with only smooth ejecta entering the shock. However, no simulations have been performed with the shock parameters and cooling functions derived here. At this time, the complete shell

of X-ray, radio, and optically emitting ejecta appears to demand a range of input densities as noted.

Planar shock models calculate the cooling times and distances of the shocked ejecta. The actual three-dimensional situation is more complicated, as hydrodynamic simulations show, but the planar models, which contain a fuller treatment of the radiation transport, help to guide our understanding of the emission we observe. The models in GRID-1E6 for shock velocities of 20–200 km s^{-1} contribute most of the optical emission to the combined spectrum. The cooling times (the time it takes the postshock gas to cool to $\sim 1000 \text{ K}$) range from only days to several months, and the corresponding cooling distances range from < 0.1 to 1 AU (relative to the shock; see also the discussion in Sutherland & Dopita 1995). These attributes lead us to infer the following about the optically emitting ejecta in the PRSS of Cas A. First, photometric variations in the ejecta, such as the “sudden” appearance or complete disappearance of knots and filaments over the interval between our observations, are a natural consequence of the short cooling times of the metal-rich gas. Second, emission that persists for years reflects the timescale for the shock to propagate across the ejecta clumps. For example, for an ejecta clump $0''.2 = 1 \times 10^{16} \text{ cm}$ thick, a 100 km s^{-1} shock takes $\sim 30 \text{ yr}$ to traverse the clump (the cloud crushing time), consistent with the optical fading time observed for many FMKs in Cas A (e.g., van den Bergh & Kamper 1983, 1985).

Our measurements of the RS parameters in Cas A show it to be generally expanding outward at 50%–60% of the free expansion velocity of the ejecta (inward in the reference frame of the expanding ejecta). Eventually, when the forward shock has swept up sufficient mass relative to the ejecta mass, the RS will accelerate to the center of the SNR. Such a situation may

be occurring in the older (~ 2500 yr) O-rich remnant N132D in the Large Magellanic Cloud. The N132D outer blast wave is impacting a dense circumstellar shell with an estimated swept-up mass of $300\text{--}600 M_{\odot}$ (Hughes 1987; Morse et al. 1996), while the RS excites several O-rich filaments near the SNR center. As such, N132D may foreshadow the future evolution of Cas A.

5. CONCLUSIONS

We have observed the Cas A SNR with the WFPC2 instrument aboard the *HST* in 2000 January and 2002 January in broad filters that capture bright optical emission over the entire velocity range of the fast-moving ejecta. The images provide many new insights into the fine-scale structure and dynamics of the remnant. In this paper, we have used the two epochs to trace the motions of the optical knots and to identify rapid line emission changes expected in shocked metal-rich gas.

1. At nearly every location around the main SNR shell where optical ejecta are observed, some form of emission variation is seen. In some cases, new emission features are seen in the 2002 images that were not present in the 2000 exposures. These are generally in the form of new knots associated with larger emission complexes, which we interpret to result from additional ejecta material associated with these large networks having crossed the reverse shock (RS). In other cases, the emitting filaments change flux (usually decreasing) or shape, while in a few locations the ejecta knots have disappeared completely in the second epoch.

2. We focus on regions in the northwest and southwest outer rims where our viewing geometry is roughly edge-on to show the location of the RS. New features emerge from a thin interface at each location and begin to radiatively cool. The interface appears coherent over arcminute scales transverse to the expansion direction but does not evolve uniformly. The RS

interface generally expands outward at roughly half the expansion velocity of the ejecta, but the RS appears to stagnate in some locations at arcsecond scales. Such differential evolution would naturally lead to the highly contorted appearance of the RS.

3. We use grids of planar shock models to estimate the range of gas densities and shock velocities in the optically emitting ejecta. Preshock densities of $25\text{--}2500 \text{ cm}^{-3}$ and shock velocities of $20\text{--}200 \text{ km s}^{-1}$ are needed to reproduce the optical emission-line ratios. These contrast with the average density of $\sim 0.25 \text{ cm}^{-3}$ and shock velocity of $\sim 2000 \text{ km s}^{-1}$ at the RS that we estimate for the X-ray-emitting gas based on ram pressure arguments. Thus the optical knots represent the peak in a likely continuous distribution of gas densities in the expanding SN debris. The low covering fraction of the optical knots and the filamentary appearance of both the optical and X-ray-emitting gas highlighted in previous studies suggest that the expanding debris may resemble a “sponge” over large scales, with high-density walls or rings at the boundaries between mostly low-density bubble-like structures.

Further high-resolution *HST* images may help to clarify the global structure, location, and velocity variations of the Cas A RS. In particular, images taken less than 2 yr apart may provide better constraints on the postshock cooling timescales and RS velocities.

J. M. thanks J. Hester, U. Hwang, J. Raymond, and J. Hughes for helpful discussions. We also thank T. DeLaney for discussions of the optical, X-ray, and radio alignment. This work was supported by grants HST-GO-8281.01-97A to Dartmouth College, HST-GO-8281.02-97A to the University of Colorado, HST-GO-8281.07A to Arizona State University, and NSF-AST-0307366 to the University of Virginia.

REFERENCES

- Anderson, M. C., & Rudnick, L. 1995, *ApJ*, 441, 307
 Arendt, R. G., Dwek, E., & Moseley, S. H. 1999, *ApJ*, 521, 234
 Blair, W. P., Raymond, J. C., Danziger, J., & Matteucci, F. 1989, *ApJ*, 338, 812
 Blair, W. P., Raymond, J. C., & Long, K. S. 1994, *ApJ*, 423, 334
 Blair, W. P., et al. 2000, *ApJ*, 537, 667
 Blondin, J. M. 2001, in *AIP Conf. Proc.* 565, *Young Supernova Remnants*, ed. S. S. Holt & U. Hwang (New York: AIP), 59
 Blondin, J. M., Borkowski, K. J., & Reynolds, S. P. 2001, *ApJ*, 557, 782
 Borkowski, K., & Shull, J. M. 1990, *ApJ*, 348, 169
 Borkowski, K., Szymkowiak, A. E., Blondin, J. M., & Sarazin, C. L. 1996, *ApJ*, 466, 866
 Chevalier, R. A. 1982, *ApJ*, 258, 790
 Chevalier, R. A., & Kirshner, R. P. 1978, *ApJ*, 219, 931
 ———. 1979, *ApJ*, 233, 154
 DeLaney, T., & Rudnick, L. 2003, *ApJ*, 589, 818
 DeLaney, T., Rudnick, L., Fesen, R. A., Jones, T. W., Petre, R., & Morse, J. A. 2004, *ApJ*, 613, 343
 Dopita, M. A., Binette, L., & Tuohy, I. R. 1984, *ApJ*, 282, 142
 Fesen, R. A. 2001, *ApJS*, 133, 161
 Fesen, R. A., & Becker, R. H. 1991, *ApJ*, 371, 621
 Fesen, R. A., Becker, R. H., & Blair, W. P. 1987, *ApJ*, 313, 378
 Fesen, R. A., Morse, J. A., Chevalier, R. A., Borkowski, K. J., Gerardy, C. L., Lawrence, S. S., & van den Bergh, S. 2001, *AJ*, 122, 2644
 García-Segura, G., Langer, N., & Mac Low, M.-M. 1996, *A&A*, 316, 133
 Gotthelf, E., Koralesky, B., Rudnick, L., Jones, T., Hwang, U., & Petre, R. 2001, *ApJ*, 552, L39
 Hartigan, P., Morse, J. A., & Raymond, J. 1994, *ApJ*, 436, 125
 Hughes, J. P. 1987, *ApJ*, 314, 103
 Hughes, J. P., Rakowski, C. E., Burrows, D. N., & Slane, P. O. 2000, *ApJ*, 528, L109
 Hurford, A. P., & Fesen, R. A. 1996, *ApJ*, 469, 246
 Itoh, H. 1981, *PASJ*, 33, 1
 ———. 1986, *PASJ*, 38, 717
 Langer, N., & El Eid, M. F. 1986, *A&A*, 167, 265
 Lawrence, S. S., MacAlpine, G. M., Uomoto, A., Woodgate, B. E., Brown, L. W., Oliverson, R. J., Lowenthal, J. D., & Liu, C. 1995, *AJ*, 109, 2635
 Morse, J. A., et al. 1996, *AJ*, 112, 509
 Murray, S., Ransom, S. M., Juda, M., Hwang, U., & Holt, S. S. 2002, *ApJ*, 566, 1039
 Peimbert, M., & van den Bergh, S. 1971, *ApJ*, 167, 223
 Reed, J. E., Hester, J. J., Fabian, A. C., & Winkler, P. F. 1995, *ApJ*, 440, 706
 Schaeffer, R., Cassé, M., & Cahen, S. 1987, *ApJ*, 316, L31
 Sutherland, R. S., Bicknell, G. V., & Dopita, M. A. 1993, *ApJ*, 414, 510
 ———. 2003, *ApJ*, 591, 238
 Sutherland, R. S., & Dopita, M. A. 1995, *ApJ*, 439, 381
 Tananbaum, H. 1999, *IAU Circ.* 7246
 Thorstensen, J. R., Fesen, R. A., & van den Bergh, S. 2001, *AJ*, 122, 297
 Vancura, O., Blair, W. P., Long, K. S., & Raymond, J. C. 1992, *ApJ*, 394, 158
 van den Bergh, S., & Kamper, K. W. 1983, *ApJ*, 268, 129
 ———. 1985, *ApJ*, 293, 537
 Vink, J., Kaastra, J. S., & Bleeker, J. A. M. 1996, *A&A*, 307, L41